Physicochem. Probl. Miner. Process., 62(4), 2026, 226745

http://www.journalssystem.com/ppmp

Physicochemical Problems of Mineral Processing

ISSN 1643-1049

Process mineralogical characteristics and electronic structures of zinc-bearing phases in electric arc furnace dust

Shengtao He [1], Jinxia Zhang [12], Yueshan Gao [1], Chao Yang [1], Yukun An [1], Fusheng Niu [1,2]

[1] College of Mining Engineering, North China University of Science and Technology, Tangshan 063210, Hebei, China

[2] Collaborative Innovation Center of Green Development and Ecological Restoration of Mineral Resources, Tangshan 063210, Hebei, China

Corresponding authors: niufusheng@ncst.edu.cn (Fusheng Niu), kyky@ncst.edu.cn (Jinxia Zhang)

Abstract: This study combined X-ray fluorescence spectroscopy (XRF), inductively coupled plasma optical emission spectrometry (ICP-OES), X-ray diffraction (XRD), mineral liberation analysis (MLA), scanning electron microscopy-energy-dispersive X-ray spectroscopy (SEM-EDS), and density functional theory (DFT) to characterize zinc-bearing constituents in electric arc furnace (EAF) dust from a steel plant in Hebei, China, across multiple length scales. ICP-OES gave Zn and Fe contents of 33.48 and 19.05 wt.%, respectively, in general agreement with the XRF results. Screening semi-quantification by XRD-RIR indicated that the relative contents of the Zn-bearing Fe-based spinel-type oxide group, ZnO, and KCl among the identified crystalline phases were 81.3%, 15.2%, and 3.5%, respectively. Because the diffraction peaks of several spinel endmembers overlap, the first value does not represent the abundance of pure $ZnFe_2O_4$. MLA assigned a calculated mass fraction of 67.96 wt.% to the spinel-type Zn-Fe oxide class and 76.57% of Zn to this operational class. SEM-EDS of selected regions showed that the spinel-type Zn-Fe oxide class was dominated by Zn and Fe, whereas the Mg-bearing Zn-rich composite oxide class contained Zn, Mg, Ca, and Fe; both classes showed non-stoichiometric, multicomponent characteristics. Fine-particle attachment and agglomeration observed by SEM indicate that some coarse MLA objects may correspond to fine-grained intergrowths or agglomerates. DFT comparison of ideal $ZnFe_2O_4$ and ZnO structural endmembers showed that the Fe-O network contributes substantially to framework stability in the spinel model and that the two structures differ in their local atomic-force responses to vacancy perturbations. The resulting framework integrates bulk phase confirmation, particle-scale occurrence, and atomic-scale structural comparison, providing a structural basis for future activation and selective recovery of zinc-bearing phases.

***Keywords*:** electric arc furnace dust, zinc-bearing phases, process mineralogy, mineral liberation analysis, density functional theory, electronic structure

1. Introduction

Large amounts of electric arc furnace (EAF) dust are generated during EAF steelmaking, generally at approximately 10-20 kg per tonne of crude steel produced (Sofilic et al., 2004; Machado et al., 2006). As a typical metallurgical secondary solid waste, EAF dust is characterized by high generation volume, complex composition, and enrichment of heavy metals. It commonly contains Zn, Fe, Pb, Ca, and Cl, with a relatively high Zn content, and therefore has both environmental risk and resource value (Trifunovic et al., 2022; Xue et al., 2023). Improper disposal may allow heavy metals such as Zn and Pb to contaminate soil and groundwater (Lin et al., 2017), whereas the relatively high Zn grade makes EAF dust a potentially valuable secondary zinc resource (Wang et al., 2021). Efficient separation and recovery of Zn from EAF dust are therefore important for waste minimization, environmental protection, and the green and circular development of the iron and steel industry.

Current Zn recovery routes for EAF dust mainly include pyrometallurgical treatment, hydrometallurgical leaching, and combined pyro-hydrometallurgical processes (Oustadakis et al., 2010; Borda and Torres, 2022; Khebri et al., 2025), and their performance depends strongly on the occurrence

DOI: 10.37190/ppmp/226745

state of Zn. Spinels in EAF dust are commonly compositionally variable solid solutions that may be expressed as $(Zn_xMn_\gamma Fe_{1-x-\gamma})Fe_2O_4$ and may contain Mg, Cr, and other cations, rather than pure $ZnFe_2O_4$ (Pickles, 2011). Accordingly, experimentally identified material is described here as spinel-type Zn-Fe oxide, whereas $ZnFe_2O_4$ denotes only the idealized DFT reference model.

Process mineralogy can quantify phase abundance, element distribution, particle size, intergrowth, and liberation in complex secondary resources (Hagni et al., 1991; Gu, 2003; Schulz, 2021). MLA combines backscattered-electron imaging with energy-dispersive X-ray spectra to obtain statistically based particle-scale information (Fandrich et al., 2007; Schulz et al., 2019), but remains a local, two-dimensional SEM-EDS method. It cannot uniquely distinguish stoichiometric $ZnFe_2O_4$, magnetite-based spinels, and multicomponent spinel solid solutions with similar mean EDS compositions; moreover, a coarse segmented object may be an agglomerate rather than a single crystal. MLA was therefore used together with bulk XRD and bulk chemical analysis, and agreement and disagreement among the methods are discussed explicitly.

Bulk chemical analysis, XRD, and process mineralogy reveal overall composition, crystalline phase type, and particle-scale occurrence, respectively, but do not fully resolve intrinsic differences in local bonding and defect response among crystal frameworks. Within a consistent computational framework, DFT can compare the coordination, M-O bonding, and vacancy-induced local response of ideal Zn-bearing compounds, helping to relate particle-scale interface exposure to atomic-scale structural stability (Yao et al., 2013; Meng et al., 2019; Salcedo Rodriguez et al., 2020; Rezende et al., 2022). For compositionally complex spinel-type oxides that cannot be further separated reliably by conventional XRD and EDS, stoichiometric $ZnFe_2O_4$ and ZnO can serve as ideal endmembers of the spinel framework and wurtzite structure, respectively. Their comparison identifies intrinsic structural differences and provides testable structural hypotheses for subsequent activation and leaching studies.

Published studies show substantial source-dependent variations in bulk Zn and Fe contents, ZnO/spinel proportions, particle morphology, and aggregation state in EAF dust (Hagni et al., 1991; Guézennec et al., 2005; Machado et al., 2006; Martins et al., 2008; Suetens et al., 2015; Alcaraz et al., 2020). These variations reflect differences in feed materials, furnace operation, off-gas thermal history, and dust collection. The present study first uses bulk chemical analysis and XRD to establish overall composition and major crystalline phases, then applies MLA and SEM-EDS to characterize particle-scale occurrence, liberation, boundary exposure, and local composition of the Zn-bearing constituents. Ideal $ZnFe_2O_4$ and ZnO are subsequently used as reference compounds to compare M-O bonding and atomic-force responses to vacancies. This bulk confirmation-particle occurrence-structural endmember sequence provides a basis for understanding the complex Zn-bearing phases in EAF dust and for designing subsequent separation and recovery tests.

2. Materials and methods

Approximately 50 kg of EAF dust was collected from the steelmaking dust-collection system. Immediately after sampling, the material was placed in double-sealed polyethylene bags and stored at room temperature under dry, dark conditions. The bulk sample was thoroughly homogenized by coning and then repeatedly reduced by quartering to an approximately 1 kg laboratory sample. Before each analytical subsample was taken, the laboratory sample was remixed, after which separate portions were obtained for chemical analysis, XRD, and MLA.

2.1. Chemical analysis

The bulk elemental composition was first screened using a handheld X-ray fluorescence spectrometer (XRF; Thermo Scientific Niton XL2 Scientific, USA), and metallic elements were independently quantified using an inductively coupled plasma optical emission spectrometer (ICP-OES; Thermo Fisher Scientific iCAP 7600, USA). Sample preparation followed the approach of Machado et al. (2006). A 0.40 g portion was treated sequentially with 3 mL HCl, 5 mL HNO_3, and 1 mL HF and microwave-digested at 600 W for 45 min. After solid-liquid separation, the acid-soluble fraction was transferred to a 100 mL volumetric flask and diluted to volume. The insoluble residue was mixed with 1.0 g $Na_2B_4O_7 \cdot 10H_2O$, fused at 1050 °C for 20 min, cooled, dissolved in 25 mL HCl, and diluted to 100 mL. The acid digest and the solution obtained from residue fusion were analyzed separately by ICP-OES,

and the two results were combined to obtain the total contents of Zn, Fe, Ca, Mg, and the other measured metallic elements. XRF was used for elemental screening and auxiliary comparison, whereas quantitative discussion of metallic elements was based on ICP-OES.

2.2. XRD analysis

An EAF-dust portion obtained after thorough homogenization and splitting was analyzed by X-ray diffraction using a Shimadzu XRD-6000 diffractometer with Cu Kα radiation ($K\alpha_1$, λ = 1.5406 Å). The tube voltage and current were 40 kV and 40 mA, respectively; the scan range was 5°-90° (2θ), with a step size of approximately 0.02°. Crystalline phases were matched from their characteristic diffraction peaks against standard patterns, and the reference intensity ratio (RIR) method was used for screening semi-quantification of the principal crystalline phase groups (Chung, 1974).

2.3. MLA and SEM-EDS analyses

The MLA system comprised an FEI scanning electron microscope, an EDAX energy-dispersive spectrometer, and MLA650 automated mineral-analysis software. Before mount preparation, the approximately 1 kg laboratory sample was thoroughly remixed, and a 1.0 g analytical subsample was obtained by staged splitting rather than by direct surface scooping to minimize size and density segregation. The subsample was added gradually to epoxy resin and mechanically stirred at approximately 300 rpm for 3 min to distribute particles throughout the resin. This mixing step was intended to improve spatial distribution within the mount; no separate ultrasonic treatment, chemical dispersant, or dry deagglomeration procedure was applied before embedding. After curing, the mount was ground, polished, cleaned, dried, and carbon-coated. A total of 11,607 two-dimensional particle objects were identified and counted on the analyzed polished section, with a cumulative projected object area of approximately 14.56 mm² in the MLA particle layer. Operational classes were established from backscattered-electron images and EDS spectra, and their calculated mass fractions, element distributions, two-dimensional apparent sizes, liberation, and intergrowth were quantified. Morphology and local composition of the principal Zn-bearing classes were further examined using a Bruker XFlash 6|30 EDS detector at an accelerating voltage of 20 kV.

2.4. DFT calculation methods

First-principles calculations were performed for ideal normal-spinel $ZnFe_2O_4$ and wurtzite ZnO using the CASTEP module of Materials Studio. Exchange-correlation energy was treated with the GGA-PBE functional (Perdew et al., 1996), and ionic core-valence electron interactions were described using ultrasoft pseudopotentials. The plane-wave cutoff energy was 380 eV. Brillouin-zone integration employed Monkhorst-Pack sampling (Monkhorst and Pack, 1976): the k-point meshes were 4 × 4 × 4 and 2 × 2 × 1 for bulk and surface $ZnFe_2O_4$ models, respectively, and 6 × 6 × 4 and 4 × 4 × 1 for the corresponding ZnO models. Geometry optimization used the Fine quality setting, an SCF convergence tolerance of 2.0×10^{-6} eV/atom, a maximum of 500 iterations, and density mixing for electronic minimization. $ZnFe_2O_4$(111) and ZnO(001) surface models were constructed with 15 Å vacuum layers. M-O bond lengths and Mulliken bond populations were compared after structural optimization, and Zn, Fe, and O vacancies were introduced to examine atomic-force responses in defective configurations. Ideal $ZnFe_2O_4$ and ZnO were used as reference endmembers of the spinel framework and wurtzite structure, respectively.

3. Results and discussion

3.1. Chemical characterization

X-ray fluorescence spectroscopy (XRF) and inductively coupled plasma optical emission spectrometry (ICP-OES) were used to cross-check the bulk chemical composition of the EAF dust. XRF provided rapid screening over a relatively broad element range, and the instrument's direct elemental-channel results are listed in Table 1.

XRF showed that Zn and Fe were the most abundant metallic elements, at 33.82 and 18.04 wt.%, respectively, giving a Zn/Fe mass ratio of 1.87. The sample also contained Ca (2.75 wt.%), Cl (3.12 wt.%),

Mn (1.02 wt.%), K (0.97 wt.%), Pb (0.54 wt.%), and S (0.48 wt.%), together with minor Cr and Al. Table 2 presents the bulk ICP-OES results obtained after acid digestion and residue fusion and used for independent quantification of Zn, Fe, Ca, Mn, Mg, Pb, Cr, and Al.

Table 1. XRF elemental composition of the EAF dust

Element	Content (wt.%)	±2σ (wt.%)	Element	Content (wt.%)	±2σ (wt.%)
Zn	33.82	1.36	Mg	0.78	0.031
Fe	18.04	0.34	Pb	0.54	0.035
Ca	2.75	0.083	S	0.48	0.019
Cl	3.12	0.051	Si	0.24	0.026
Mn	1.02	0.040	Cr	0.14	0.019
K	0.97	0.031	Al	0.12	0.015

Note: The reported uncertainties are the instrument-displayed ±2σ values and are not standard deviations from replicate measurements. All concentrations are direct outputs from the elemental channels and were not normalized to 100%. The instrument-displayed balance (Bal) was an unquantified remainder and is not listed as a single chemical component.

Table 2. ICP-OES elemental composition of the EAF dust

Element	Content (wt.%)	Element	Content (wt.%)
Zn	33.48	Mn	1.73
Fe	19.05	Pb	0.59
Ca	6.05	Al	0.34
Mg	1.68	Cr	0.25

Note: Only the elements quantified in the present ICP-OES analysis are listed. Results are expressed as elemental mass fractions and were not normalized to 100%.

ICP-OES gave Zn and Fe concentrations of 33.48 and 19.05 wt.%, respectively. Their absolute differences from the XRF values were 0.34 and 1.01 percentage points, showing general agreement between the two methods for the principal elements. XRF values for Ca, Mg, and Mn (2.75, 0.78, and 1.02 wt.%, respectively) were lower than the corresponding ICP-OES results (6.05, 1.68, and 1.73 wt.%). These differences may reflect the calibration mode of the handheld XRF instrument, matrix effects in the complex powder, and lower sensitivity to relatively light elements. ICP-OES results were therefore used as the quantitative basis for bulk metallic elements, whereas XRF supplied complementary information on Cl, K, and S.

The ICP-OES results give a Zn/Fe mass ratio of 1.76, substantially higher than the theoretical value of 0.585 for stoichiometric $ZnFe_2O_4$; even if all Fe formed this ideal endmember, it could not accommodate all Zn in the sample. Machado et al. (2006) reported 9.24-12.00 wt.% Zn and 42.00-48.96 wt.% Fe in two EAF dusts. Holloway and Etsell (2008) reported 9.40 wt.% Zn and 31.90 wt.% Fe, whereas Pasquoto et al. (2018) reported Zn/Fe values of 37.50/25.80 wt.% and 28.60/56.10 wt.% for two samples. Relative to these materials, the present sample is distinctly Zn-rich and comparatively Fe-poor. This bulk ratio documents Zn enrichment but cannot by itself identify the Zn hosts or determine individual phase abundances.

3.2. XRD analysis

The XRD pattern of the EAF dust is shown in Fig. 1. The major discernible crystalline phases or phase groups were a Zn-bearing Fe-based spinel-type oxide, zinc oxide (ZnO; zincite), and potassium chloride (KCl; sylvite). Strong signals from ZnO and spinel-type oxides show that these are the principal

crystalline Zn-bearing constituents, while KCl is consistent with the K and Cl detected by bulk chemical analysis.

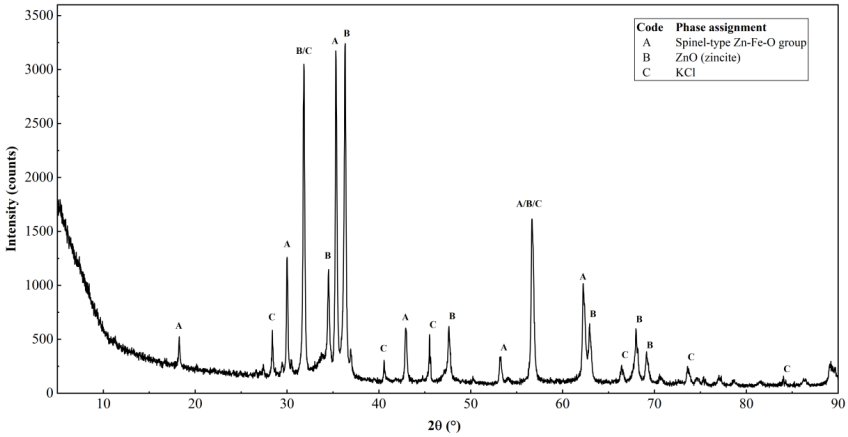

Fig. 1. XRD pattern of the EAF dust

The three discernible crystalline phase groups were screened semi-quantitatively using the RIR method and normalized to the total identified crystalline phases (Table 3). The Zn-bearing Fe-based spinel-type oxide group accounted for 81.3 wt.%, exceeding ZnO (15.2 wt.%) and KCl (3.5 wt.%), and thus indicating pronounced enrichment of spinel-type crystalline material.

Table 3. Screening XRD semi-quantification of the principal crystalline phases in the EAF dust.

Code	Phase or phase group	Relative content (wt.%)
A	Zn-bearing Fe-based spinel-type oxide	81.3
B	ZnO (zincite)	15.2
C	KCl (sylvite)	3.5

$ZnFe_2O_4$, Fe_3O_4, and multication spinel solid solutions containing Mg, Mn, Cr, and other elements have similar crystal structures and overlapping characteristic peaks, making their individual endmembers difficult to distinguish reliably by conventional XRD. Phase group A is therefore reported collectively as a Zn-bearing Fe-based spinel-type oxide group. Its semi-quantitative value represents overlapping spinel phases rather than the mass fraction of pure $ZnFe_2O_4$.

The crystalline phase composition of EAF dust varies substantially among sources. Alcaraz et al. (2020) reported nominal $ZnFe_2O_4$ and ZnO contents of 75% and 20% in carbon-steel EAF dust. Pasquoto et al. (2018) reported corresponding values of 37.0% and 31.4% for one sample and 66.8% and 11.0% for another, whereas Machado et al. (2006) estimated approximately 29% and 2%. The present sample has a relatively high abundance of the spinel phase group, while ZnO lies within the published range. Differences may reflect feed materials, smelting and gas-cleaning conditions, and phase-classification protocols. Because the present analysis combines several spinel constituents that conventional XRD cannot separate, its value should not be equated strictly with literature results refined as pure $ZnFe_2O_4$.

3.3. MLA and SEM-EDS analyses

MLA assigned a calculated mass fraction of 67.96 wt.% to the spinel-type Zn-Fe oxide class, followed by the Mg-bearing Zn-rich composite oxide class (15.23 wt.%), calcite (4.58 wt.%), Zn-Fe-Ca oxide (2.63 wt.%), and Zn-Fe-Al oxide (2.27 wt.%); the ZnO class accounted for 1.50 wt.%. Because the MLA classes were established primarily from BSE brightness and EDS spectra, the spinel-type Zn-Fe oxide class may include spinel-related Zn-Fe oxides of different compositions as well as mixed classification objects formed by fine ZnO or other intergrown oxides.

Both XRD and MLA identify spinel-related Zn-Fe oxides as the dominant component. The XRD-RIR value of 81.3 wt.% is the relative abundance of the spinel phase group normalized to the identified crystalline phases, whereas the MLA value of 67.96 wt.% is a calculated mass fraction assigned to an operational class within the MLA dataset. The former is based on crystal structure and the latter on particle-scale chemical classification, so the two quantities are not directly equivalent. The XRD ZnO value (15.2 wt.%) is higher than the MLA class value (1.50 wt.%), possibly because fine ZnO attached to Zn-Fe oxides or intergrown with other fine constituents was incorporated into mixed EDS classes. Two-dimensional sectioning and the uncertainty of screening RIR semi-quantification may also contribute. The methods therefore agree on the dominant Zn-bearing constituent but differ in their specific allocation of ZnO and complex composite oxides.

Table 4. MLA operational classes and calculated mass fractions in the EAF dust (wt.%).

Class	Spinel-type Zn-Fe oxide	Mg-bearing Zn-rich composite oxide	Calcite	Zn-Fe-Ca oxide	Zn-Fe-Al oxide	Hematite	Calcium ferrite
Content	67.96	15.23	4.58	2.63	2.27	1.61	1.38
Class	ZnO	MgO	Zn-bearing dolomite	Quartz	Zn-Fe-Mg oxide	Ca-Fe pyroxene	Zn-Fe silicate
Content	1.50	0.76	0.47	0.27	0.25	0.20	0.16
Class	Zn-Fe-Ca silicate	Zn-Mg silicate	Anorthite	Albite	Zn-Ca silicate		
Content	0.16	0.16	0.11	0.11	0.10		

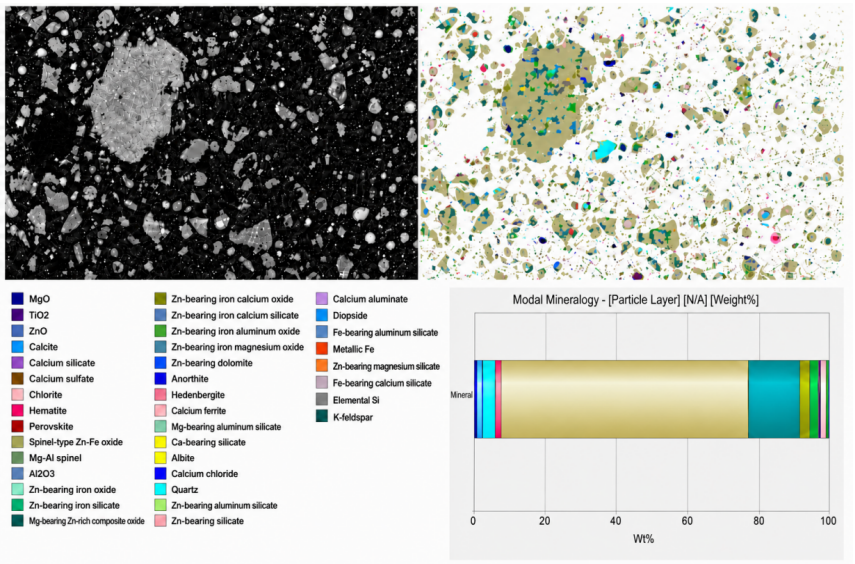

Fig. 2. MLA class composition and distribution characteristics of the EAF dust.

The BSE image and MLA phase map in Fig. 2 show irregular particles with a broad two-dimensional apparent size distribution. Coarser objects were assigned mainly to the spinel-type Zn-Fe oxide class, whereas the Mg-bearing Zn-rich composite oxide, Zn-Fe-Ca oxide, and Zn-Fe-Al oxide classes commonly occurred near particle margins, cracks, or pores, reflecting compositional heterogeneity and fine-scale intergrowth. This spatial distribution may be associated with local enrichment of multication constituents, attachment of fine particles, entrainment of slag droplets or flux particles, and subsequent reactions during off-gas transport. Some coarse objects are internally heterogeneous in BSE brightness or classification and may comprise sintered particles or weakly bound fines. MLA size is therefore

interpreted as the two-dimensional apparent size of segmented objects rather than the actual size of individual crystals.

The coexistence of coarse Zn-Fe oxide objects, fine Zn-rich particles, irregular fragments, and porous aggregates is consistent with multiple EAF-dust formation pathways. Zn may volatilize from the bath or feed and subsequently oxidize and condense as fine ZnO in the off-gas. Metal and slag droplets may be ejected by the electric arc, oxygen jets, and bursting CO bubbles, while charged fines can be entrained directly. During transport and collection, particles may undergo further oxidation, reaction, coalescence, and agglomeration (Guézennec et al., 2005). The observed morphologies provide qualitative support for this integrated mechanism, but do not permit a unique formation pathway to be assigned to an individual object.

3.3.1. Element occurrence

Table 5 lists the distributions of Fe, Ca, Mg, and Zn among the operational classes within the MLA analysis area. Zn was distributed mainly to the spinel-type Zn-Fe oxide and Mg-bearing Zn-rich composite oxide classes, at 76.57% and 16.95%, respectively; together they accounted for 93.52% of total Zn. The ZnO class hosted 1.94% of total Zn. At the MLA classification scale, Zn therefore occurs predominantly in Zn-Fe- and Zn-Mg-related composite oxide objects.

The spinel-type Zn-Fe oxide class hosted 67.61% of Fe, while the Mg-bearing Zn-rich composite oxide, Zn-Fe-Al oxide, and Zn-Fe-Ca oxide classes hosted 9.85%, 5.37%, and 3.75%, respectively. Fe was thus concentrated mainly in several types of Zn-bearing composite oxides. Mg was distributed chiefly to the Mg-bearing Zn-rich composite oxide (63.91%) and MgO (17.98%) classes. Ca was concentrated in calcite (37.80%), with 27.64% and 12.41% also assigned to the spinel-type Zn-Fe oxide and Zn-Fe-Ca oxide classes, respectively.

The cross-distribution of Fe, Ca, and Mg among several Zn-bearing classes reflects compositional heterogeneity and fine-scale intergrowth within the major Zn-bearing objects. Possible contributions include coexistence of multication constituents, intergrowth with Ca- or Mg-rich microphases, and mixed signals within the EDS interaction volume. Overall, Zn is enriched in complex oxide objects dominated by Zn-Fe and Zn-Mg components rather than in a single ideal stoichiometric endmember.

Table 5. Distribution of major elements among the MLA operational classes (%)

Class	Fe	Ca	Mg	Zn
Spinel-type Zn-Fe oxide	67.61	27.64	0.97	76.57
Mg-bearing Zn-rich composite oxide	9.85	7.56	63.91	16.95
Hematite	6.48	1.42	2.99	0
Zn-Fe-Al oxide	5.37	0.99	0.74	1.76
Zn-Fe-Ca oxide	3.75	12.41	2.10	1.05
Calcium ferrite	3.17	6.53	1.26	0.12
Calcite	2.01	37.80	0.53	1.00
ZnO	0.59	0.31	-	1.94
Ca-Fe pyroxene	0.27	0.54	0.14	0.02
Zn-bearing dolomite	0.25	2.28	4.06	0.11
Zn-Fe-Mg oxide	0.13	0.03	2.66	0.15
MgO	-	0.03	17.98	0.01
Zn-Mg silicate	0.02	0.75	1.87	0.01
Other	0.50	1.71	0.79	0.31
Total	100	100	100	100

3.3.2. Apparent particle-size distribution

The apparent size distributions of the MLA-segmented objects are shown in Fig. 3. These data describe two-dimensional objects on a polished section and may include primary particles, composite particles, and agglomerates.

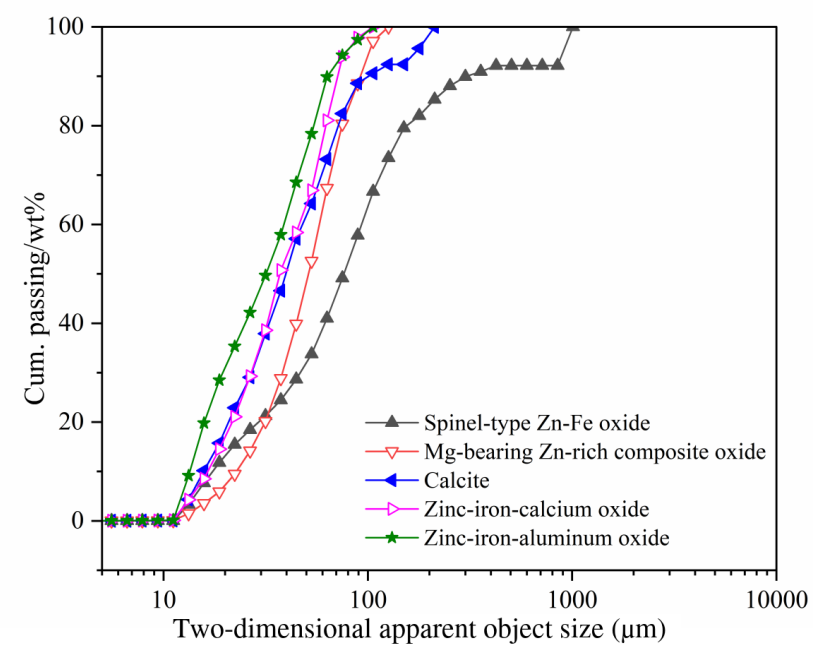

Fig. 3. Two-dimensional apparent size distributions of the principal MLA operational classes

Fig. 3 shows that the two-dimensional apparent size distribution of the spinel-type Zn-Fe oxide class is shifted toward the coarse-size range and spans a comparatively broad interval, indicating that this class commonly forms larger segmented objects. In contrast, the Mg-bearing Zn-rich composite oxide, Zn-Fe-Ca oxide, and Zn-Fe-Al oxide classes occur mainly in finer size ranges and commonly form small objects or localized enriched regions. These differences describe the relative object sizes and spatial distributions of the operational classes on the polished section.

3.3.3. Representative SEM-EDS compositions and morphological features

To characterize local composition and morphology, the two most abundant Zn-bearing operational classes, the spinel-type Zn-Fe oxide class (67.96 wt.%) and the Mg-bearing Zn-rich composite oxide class (15.23 wt.%), were selected for BSE observation and EDS point analysis. High-magnification SEM imaging of unmounted powder was also used to examine fine-particle morphology and aggregation. Points G-I and A-F are indicated in Figs. 4a and 4b, respectively, and Fig. 4c shows the high-magnification surface morphology of the unmounted powder.

The BSE images in Figs. 4a and 4b show that coarse objects commonly have irregular or near-rounded outlines and marked internal brightness variations. The area in Fig. 4c comprises submicrometre spherical, near-spherical, and irregular fine particles. Finer particles adhere to the surfaces of some larger particles and form agglomerates with irregular boundaries, demonstrating a multiscale particle structure and pronounced agglomeration. These features are consistent with fine-particle aggregates reported for EAF dust by Guézennec et al. (2005) and Suetens et al. (2015). Near-spherical particles may be associated with vapour-phase condensation or droplet solidification, whereas irregular particles may originate from entrained droplets or charged fines; coalescence and local sintering during off-gas transport and collection may further promote agglomeration.

Normalized EDS results for points A-F and G-I are listed in Tables 6 and 7, respectively, to compare the local compositions of regions with different BSE brightness. Zn and Fe were the major metallic elements at A-F, with minor Ca and Mn. Points G-I were enriched in both Zn and Mg and also contained Ca and Fe, indicating compositional heterogeneity within both classes.

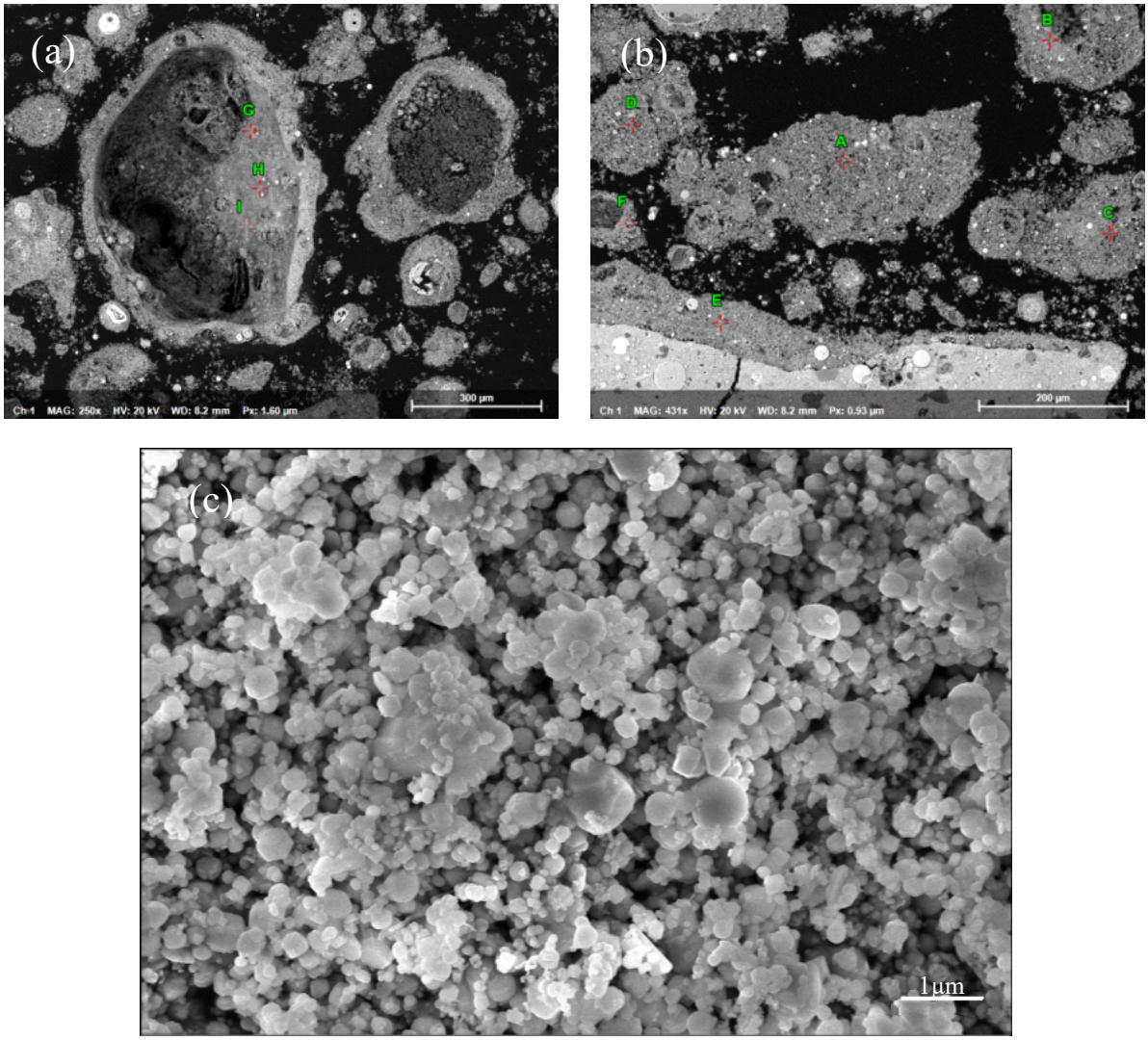

Fig. 4. Representative SEM morphologies and EDS point locations in the EAF dust: (a) points G-I in the Mg-bearing Zn-rich composite oxide class (BSE); (b) points A-F in the spinel-type Zn-Fe oxide class (BSE); and (c) aggregates of fine spherical, near-spherical, and irregular particles (SE)

Table 6. Normalized EDS compositions of the spinel-type Zn-Fe oxide class (wt.%)

Point	O	Ca	Mn	Fe	Zn	Zn/Fe atomic ratio
A	8.80	2.25	1.77	24.87	62.31	2.14
B	10.54	3.18	1.56	23.43	61.29	2.23
C	12.63	1.69	1.36	20.04	64.28	2.74
D	11.69	1.89	1.63	26.84	57.95	1.84
E	10.47	1.60	1.33	22.48	64.12	2.44
F	10.73	2.36	1.59	21.99	63.33	2.46
Mean	10.81	2.16	1.54	23.28	62.21	≈2.3

Zn and Fe were the principal metallic elements at all points A-F, ranging from 57.95 to 64.28 wt.% and from 20.04 to 26.84 wt.%, respectively, together with minor Ca (1.60-3.18 wt.%) and Mn (1.33-1.77 wt.%). The Zn/Fe atomic ratios of 1.84-2.74 are substantially higher than the theoretical value of 0.50

for stoichiometric $ZnFe_2O_4$, demonstrating pronounced Zn enrichment and precluding simple assignment of these regions to ideal stoichiometric $ZnFe_2O_4$. Together with internal BSE-brightness differences, the data support description of this MLA class as compositionally variable, spinel-related Zn-Fe oxide. The local variations may reflect cation substitution, Zn-rich microregions, or sub-resolution intergrowth, although point EDS alone cannot distinguish these possibilities rigorously.

Table 7. Normalized EDS compositions of the Mg-bearing Zn-rich composite oxide class (wt.%)

Point	O	Mg	Ca	Fe	Zn	Zn/Mg atomic ratio
G	38.12	12.97	7.50	5.06	36.35	1.04
H	36.38	15.16	5.27	7.01	35.74	0.88
I	35.76	12.98	8.29	8.63	34.34	0.98
Mean	36.75	13.70	7.02	6.90	35.48	≈0.96

Note: G, H, and I correspond to the points in Fig. 4a; Zn/Mg atomic ratios were calculated from the normalized mass fractions.

Zn, Mg, Ca, and Fe were detected at all points G-I. Zn and Mg ranged from 34.34 to 36.35 wt.% and from 12.97 to 15.16 wt.%, respectively, with Zn/Mg atomic ratios of 0.88-1.04, indicating co-enrichment in the selected areas. The points also contained 5.27-8.29 wt.% Ca and 5.06-8.63 wt.% Fe and showed clear multication compositions and point-to-point variation. This MLA operational class is therefore described as an Mg-bearing Zn-rich composite oxide. Its local composition may represent a multication oxide or sub-resolution intergrowth of fine Zn-, Mg-, Ca-, and Fe-rich phases, rather than a single Zn-Mg oxide phase.

The selected EDS regions in both major Zn-bearing classes show multielement coexistence and within-class compositional variation, while high-magnification SEM reveals fine-particle attachment and agglomeration. A coarse MLA-segmented object does not necessarily represent a single coarse grain; it may comprise a fine-grained intergrowth or an agglomerate. The corresponding size data therefore denote two-dimensional apparent object sizes on the polished section rather than actual primary-grain sizes.

3.3.4. Intergrowth characteristics

Liberation and association statistics for the principal MLA operational classes are presented in Table 8. The reported liberation degree of the spinel-type Zn-Fe oxide class was 68.86%, higher than those of calcite (43.22%), the Mg-bearing Zn-rich composite oxide class (42.52%), and the Zn-Fe-Ca oxide class (37.75%). The spinel-type class therefore occurred more frequently as relatively independent objects on the two-dimensional polished section, whereas the Mg-bearing Zn-rich composite oxide and Zn-Fe-Ca oxide classes displayed more extensive particle contact and intergrowth.

Further examination of the remaining association terms showed that associations with Ca-bearing silicate, albite, and quartz were each no greater than 0.11%, indicating limited direct intergrowth between these silicates and the principal Zn-bearing classes. In addition to shared boundaries between mineral classes, the MLA association matrix contains non-mineral categories such as Pores and Low_Counts. When normalized to the total boundary length of the target class on the two-dimensional section, Pores associations ranged from 9.72% to 27.11%; the highest value was for calcite, followed by the Zn-Fe-Ca oxide and spinel-type Zn-Fe oxide classes. Pores denotes regions segmented as voids within or adjacent to MLA objects and may include internal voids, resin-filled gaps between contacting or agglomerated particles, and local polishing pull-outs. It therefore measures boundary association with the Pores category on a two-dimensional section and cannot be interpreted directly as the true porosity of the bulk sample (Fandrich et al., 2007; Sylvester, 2012). Low_Counts accounted for 2.52%-5.09% and primarily represents regions with insufficient effective EDS counts or spectra that could not be matched reliably to the reference library. Such regions may occur in very small mineral domains, at

mineral boundaries, in mixed excitation volumes, or near preparation artefacts and do not correspond to a defined mineral phase (Schulz et al., 2019). These liberation and association statistics characterize boundary exposure, physical liberation, and spatial contact among MLA operational classes on a two-dimensional polished section.

Table 8. Intergrowth relationships of the principal MLA operational classes (%)

Class	Liberation	Association			
		MgO	ZnO	Calcite	Hematite
Spinel-type Zn-Fe oxide	68.86	0.22	0.39	1.73	0.58
Mg-bearing Zn-rich composite oxide	42.52	0.41	0.38	1.86	0.82
Calcite	43.22	0.05	0.10	-	0.46
Zn-Fe-Ca oxide	37.75	0.01	0.18	7.16	1.06
Zn-Fe-Al oxide	50.86	0.22	0.48	1.28	1.11

Class	Association				
	Spinel-type Zn-Fe oxide	Zn-Fe silicate	Mg-bearing Zn-rich composite oxide	Zn-Fe-Ca oxide	Zn-Fe-Ca silicate
Spinel-type Zn-Fe oxide	-	0.12	7.12	1.05	0.08
Mg-bearing Zn-rich composite oxide	35.31	0.09	-	1.24	0.12
Calcite	17.31	0.04	3.75	3.28	0.05
Zn-Fe-Ca oxide	22.95	0.22	5.45	-	0.02
Zn-Fe-Al oxide	25.40	0.05	6.06	0.45	0.12

Class	Association				
	Zn-Fe-Al oxide	Zn-Fe-Mg oxide	Zn-bearing dolomite	Ca-Fe pyroxene	Calcium ferrite
Spinel-type Zn-Fe oxide	1.19	0.10	0.18	0.05	0.43
Mg-bearing Zn-rich composite oxide	1.41	0.06	0.26	0.09	0.47
Calcite	0.60	0.01	0.22	0.05	1.09
Zn-Fe-Ca oxide	0.46	0.06	0.15	0.11	2.21
Zn-Fe-Al oxide	-	0.03	0.05	0.02	0.45

Class	Association				
	Ca-bearing silicate	Albite	Quartz	Pores	Low_Counts
Spinel-type Zn-Fe oxide	0.02	0.04	0.05	13.71	4.08
Mg-bearing Zn-rich composite oxide	0.05	0.04	0.06	9.72	5.09
Calcite	0.02	0.01	0.11	27.11	2.52
Zn-Fe-Ca oxide	0.07	0.03	-	18.26	3.85
Zn-Fe-Al oxide	0.01	0.05	0.06	10.66	2.64

3.3.5. Two-dimensional free-surface characteristics

The free-surface ratio (FSR) was used to characterize boundary exposure of the different MLA classes on the two-dimensional polished section. It was defined as the boundary length between the target class and the external particle background divided by the total boundary length of that class, consistent with exposed-perimeter methods for assessing mineral liberation and surface exposure (Lastra, 2002; Fandrich et al., 2007; Leißner et al., 2016):

$$\mathrm{FSR} = \frac{L_{\mathrm{free}}}{L_{\mathrm{free}}+\Sigma_j L_j} \times 100\% \quad (1)$$

where L_{free} is the two-dimensional free-boundary length between the target class and the external particle background (mounting resin); L_j is the boundary length shared between the target class and adjacent class j; and $\Sigma_j L_j$ is the total non-free boundary length. FSR ranges from 0% to 100%, and a higher value indicates a greater proportion of the target class boundary adjoining the particle exterior on the two-dimensional section.

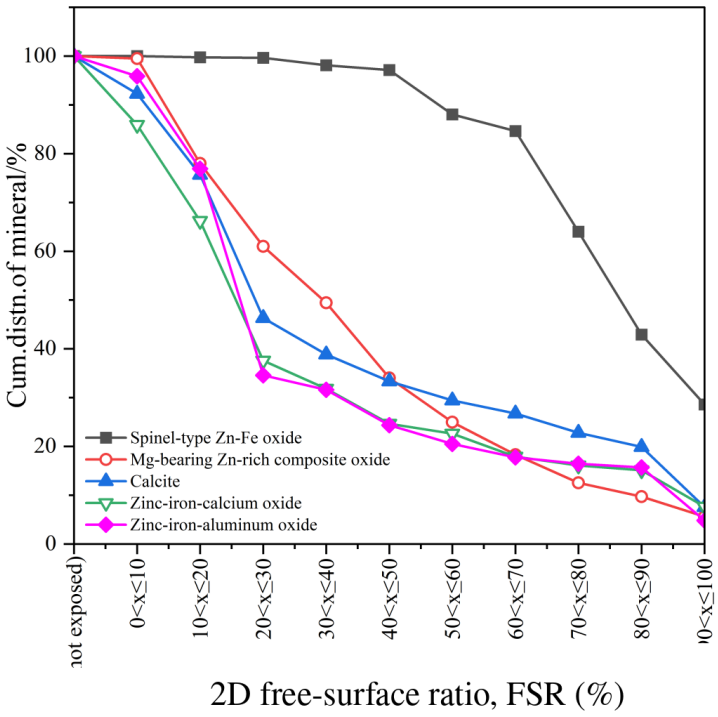

Fig. 5. Cumulative distributions of the two-dimensional free-surface ratio for the principal MLA operational classes

Fig. 5 shows that the FSR distribution of the spinel-type Zn-Fe oxide class is shifted toward higher values. The cumulative proportions of objects with FSR values above 60% and 80% were 84.61% and 42.90%, respectively, indicating a high degree of boundary exposure on the analyzed section. In contrast, the curves for the Mg-bearing Zn-rich composite oxide and Zn-Fe-Ca oxide classes are shifted toward lower FSR values, indicating greater contact with other classified materials. This trend agrees with the preceding liberation and association results.

Under conditions of adequate wetting and dispersion, greater boundary exposure can provide favourable geometry for contact and interfacial mass transfer between a target class and a reaction medium. The relatively high FSR of the spinel-type Zn-Fe oxide class thus indicates that it is not predominantly enclosed on the two-dimensional section. Phase reactivity, however, also depends on crystal framework, local bonding, and defect response. Ideal $ZnFe_2O_4$ and ZnO were therefore compared by DFT to identify intrinsic structural differences between two representative Zn-bearing oxides and to provide an atomic-scale reference for the stability of actual multication spinel-type oxides. The effects of elemental substitution and real defects must still be considered when extrapolating the results.

3.4. Electronic-structure calculations for Zn-bearing phases in EAF dust

Ideal normal-spinel $ZnFe_2O_4$ and wurtzite ZnO were selected as reference compounds to compare M-O bonding and atomic-force responses to vacancies at the atomic scale. These models represent ideal endmembers of the spinel framework and ZnO lattice and complement the preceding particle-scale liberation and boundary-exposure results by providing an atomic-scale reference for intrinsic structural stability. Multication substitution, inversion, and other defects in actual EAF-dust phases may alter the numerical results; the following comparison is therefore restricted to the basic structural differences between ideal endmembers.

3.4.1. Crystal structures and model construction

The geometrically optimized ideal $ZnFe_2O_4(111)$ and ZnO(001) surface configurations obtained using the parameters in Section 2.4 are shown in Fig. 6.

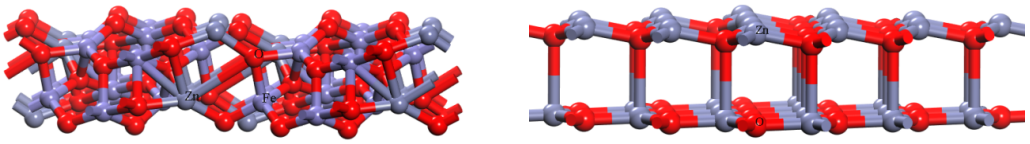

(a) $ZnFe_2O_4(111)$ (b) ZnO(001)

Fig. 6. Geometrically optimized surface configurations of ideal $ZnFe_2O_4(111)$ and ZnO(001) reference models

In ideal normal-spinel $ZnFe_2O_4$, tetrahedrally coordinated Zn and octahedrally coordinated Fe form a continuous three-dimensional framework through shared O atoms. Wurtzite ZnO consists of tetrahedrally coordinated Zn and O connected in a hexagonal sequence. Differences in cation coordination and M-O network topology provide the structural basis for comparing local bonding and vacancy responses. Spinels in actual EAF dust may contain cation substitutions, inversion, and non-stoichiometric defects and can therefore be viewed as compositionally complex derivatives of this ideal framework.

3.4.2. Comparison of M-O bond strengths

Mulliken bond population and bond length were used as descriptors to compare local bonding in the two ideal Zn-bearing oxides. Within the same computational framework, a larger positive bond population and a shorter bond length generally indicate a stronger local interaction. The comparison identifies relative bonding characteristics of the M-O networks and is not used to calculate dissolution rates or reaction activation energies directly.

Table 9. Bonding descriptors for ideal $ZnFe_2O_4(111)$ and ZnO(001) models.

Parameter	$ZnFe_2O_4(111)$ Fe-O	$ZnFe_2O_4(111)$ Zn-O	ZnO(001) Zn-O
Mean bond population	0.374	0.350	0.48
Mean bond length (Å)	1.866	2.013	1.88
Minimum bond length (Å)	1.719	1.842	1.85
Maximum single-bond population	0.65	0.55	0.54

As shown in Table 9, Fe-O bonds in the ideal $ZnFe_2O_4(111)$ model have a maximum population of 0.65 and a minimum length of 1.719 Å; their mean bond population and length are 0.374 and 1.866 Å,

respectively, indicating strong local interactions for some Fe-O bonds. The mean population and length of Zn-O bonds in the same model are 0.350 and 2.013 Å, respectively, and indicate weaker local bonding than the mean Zn-O population of 0.48 and mean length of 1.88 Å in ZnO(001). These results suggest that stability of the ideal spinel framework cannot be interpreted from Zn-O bonds alone; the continuous Fe-O network also makes an important contribution, and a perturbation at a Zn site may be accompanied by cooperative adjustment of the surrounding Fe-O coordination network.

3.4.3. Vacancy-induced atomic-force responses

Zn, Fe, and O vacancies were introduced into the $ZnFe_2O_4$(111) and ZnO(001) surface models to compare local defect responses in the two ideal structures. The corresponding structures are shown in Figs. 7 and 8, and the calculated values are listed in Table 10. Atomic force describes the departure of the local coordination environment from the original equilibrium configuration after vacancy introduction and is used here as a descriptor for comparing local responses of the ideal frameworks.

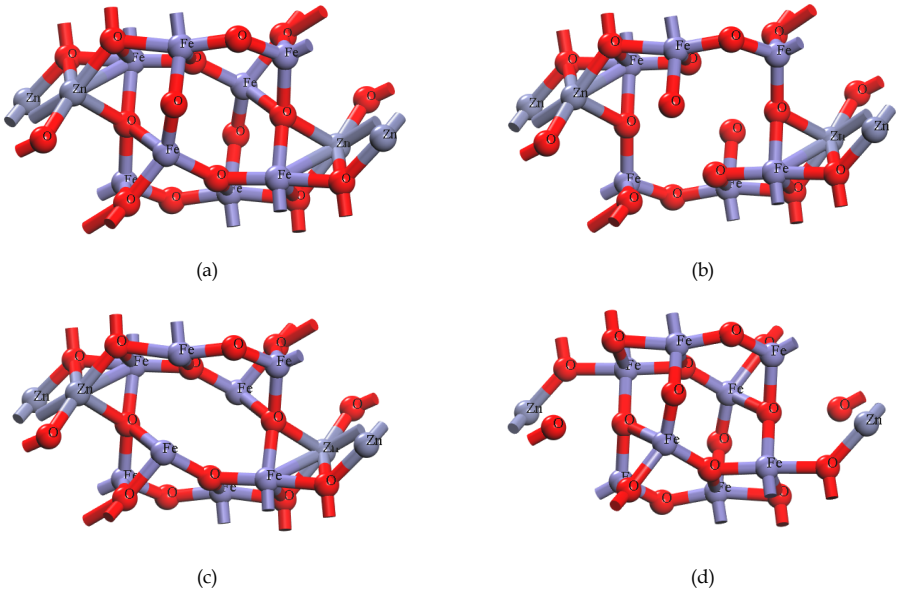

Fig. 7. Defective structures of ideal $ZnFe_2O_4$(111): (a) pristine surface; (b) V-Fe; (c) V-O; and (d) V-Zn

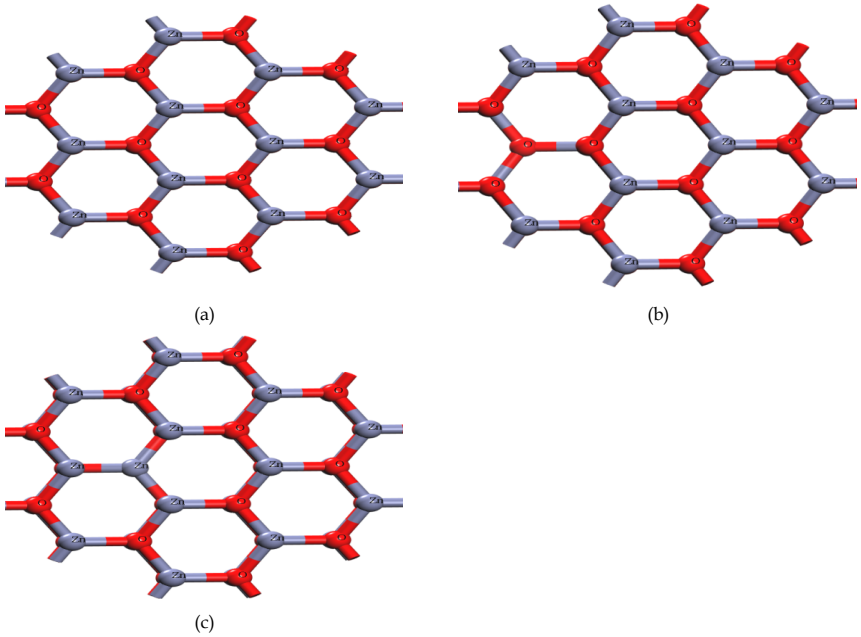

Fig. 8. Defective structures of ideal ZnO(001): (a) pristine surface; (b) V-Zn; and (c) V-O

Table 10. Atomic-force descriptors after vacancy introduction (eV/Å)

System	Mean Fe force	Mean Zn force	Mean O force	Maximum atomic force
$ZnFe_2O_4$(111) surface	0.026	0.020	0.024	0.049
ZnO(001) surface	-	0.20	0.14	1.39
$ZnFe_2O_4$ (V-Fe)	2.817	0.902	1.318	3.849
$ZnFe_2O_4$ (V-O)	0.804	0.133	0.544	1.482
$ZnFe_2O_4$ (V-Zn)	1.930	0.855	1.014	3.491
ZnO (V-O)	-	0.02	0.02	0.07
ZnO (V-Zn)	-	0.55	0.29	1.39

Table 10 shows that the maximum atomic forces in the V-Fe and V-Zn configurations of ideal $ZnFe_2O_4$(111) are 3.849 and 3.491 eV/Å, respectively, exceeding 1.482 eV/Å for V-O. The selected cation vacancies thus generate more pronounced local perturbations in the spinel framework. In the V-Zn configuration, the mean force on Fe sites (1.930 eV/Å) is higher than that on Zn sites (0.855 eV/Å), showing that removal of a Zn site induces a substantial response in the neighbouring Fe-O coordination network. By comparison, the selected vacancy configurations in ideal ZnO(001) show smaller overall force responses. These results demonstrate different local responses of the two ideal structures to cation removal and suggest that activation of a spinel framework may involve cooperative adjustment of its Fe-O network; this interpretation requires validation by subsequent experiments.

3.5. Implications for resource utilization of EAF dust

The combined bulk composition, particle-scale occurrence, and ideal-endmember calculations indicate that future valorization studies on this sample should distinguish ZnO and soluble salts from the dominant spinel-related Zn-Fe oxides. The latter show comparatively high liberation and boundary exposure on the two-dimensional section, suggesting that subsequent treatment should consider structural activation of the spinel framework in addition to particle dispersion and mass transfer. Because some coarse objects may be agglomerates of fine particles, the need for further grinding should be evaluated by comparing size and liberation before and after controlled dispersion.

The KCl and ZnO identified by XRD provide a phase basis for stepwise treatment. Water washing or mild pre-leaching may be evaluated as candidate steps for reducing the soluble-salt load and preferentially separating more reactive components. Thermal, mechanical, or chemical activation can then be coupled with different leaching media for the spinel-related fraction. The Fe-O bonding network and vacancy response in the ideal $ZnFe_2O_4$ model suggest that reaction systems capable of perturbing the cation-oxygen framework merit examination, with ZnO-rich material used as a structural and reactivity control.

Subsequent process evaluation should consider Zn extraction, Zn/Fe selectivity, reaction kinetics, reagent consumption, and residue-phase evolution, together with solution purification and residue utilization. The proposed sequence of pretreatment for burden reduction, spinel activation, selective Zn leaching, solution purification, and residue utilization follows from the present mineralogical characterization and structural-endmember comparison, but its applicability and operating conditions require validation by leaching experiments.

4. Conclusions

ICP-OES gave Zn and Fe contents of 33.48 and 19.05 wt.%, respectively, with a Zn/Fe mass ratio of 1.76, showing that the EAF dust is Zn-rich. Screening semi-quantification by XRD-RIR indicated relative abundances of 81.3%, 15.2%, and 3.5% for the Zn-bearing Fe-based spinel-type oxide group, ZnO, and KCl, respectively, among the identified crystalline phases. Spinel-related oxides were thereby

confirmed as the dominant crystalline group, but this result does not represent the mass fraction of pure $ZnFe_2O_4$.

MLA assigned a calculated mass fraction of 67.96 wt.% and 76.57% of total Zn to the spinel-type Zn-Fe oxide class. The high and variable Zn/Fe atomic ratios at points A-F and the co-enrichment of Zn, Mg, Ca, and Fe at points G-I indicate non-stoichiometric, multicomponent characteristics in the major Zn-bearing operational classes. Fine-particle attachment and agglomeration observed by SEM further indicate that coarse MLA-segmented objects may include fine-grained intergrowths or agglomerates; their sizes should therefore be interpreted as two-dimensional apparent object sizes.

The two-dimensional liberation degree of the spinel-type Zn-Fe oxide class was 68.86%, and 84.61% of the objects had FSR values above 60%, indicating comparatively high boundary exposure on the analyzed section. DFT comparison of ideal $ZnFe_2O_4$ and ZnO structural endmembers showed that the Fe-O network contributes substantially to framework stability in the spinel model and that the two structures differ in their atomic-force responses to vacancy perturbations. This endmember comparison provides an atomic-scale reference for the structural stability of actual multication spinel-type oxides and motivates subsequent validation focused on spinel activation and Zn/Fe selectivity.

Acknowledgments

This research was supported by the S&T Program of Hebei (Grant No. 25363801D), the Basic Research Program for Universities in Hebei Province (Grant No. JQN2022009), and the Tangshan Science and Technology Program (Grant No. 25150205E).

References

ALCARAZ, L., URBIETA, A., RABANAL, M.E., FERNANDEZ, P., LOPEZ, F.A., 2020. *Photocatalytic activity of electric-arc furnace flue dusts*. Journal of Materials Research and Technology 9(2), 1261–1272. DOI: 10.1016/j.jmrt.2019.11.053.

BORDA, J., TORRES, R., 2022. *Recycling of zinc and lead from electric arc furnace dust by selective leaching with EDTA*. Canadian Metallurgical Quarterly 61(4), 464–474. DOI: 10.1080/00084433.2022.2046902.

CHUNG, F.H., 1974. *Quantitative interpretation of X-ray diffraction patterns of mixtures. I. Matrix-flushing method for quantitative multicomponent analysis*. Journal of Applied Crystallography 7, 519–525. DOI: 10.1107/S0021889874010375.

FANDRICH, R., GU, Y., BURROWS, D., MOELLER, K., 2007. *Modern SEM-based mineral liberation analysis*. International Journal of Mineral Processing 84(1–4), 310–320. DOI: 10.1016/j.minpro.2006.07.018.

GU, Y., 2003. *Automated scanning electron microscope based mineral liberation analysis: An introduction to JKMRC/FEI Mineral Liberation Analyser*. Journal of Minerals and Materials Characterization and Engineering 2(1), 33–41. DOI: 10.4236/jmmce.2003.21003.

GUÉZENNEC, A.G., HUBER, J.C., PATISSON, F., SESSIECQ, P., BIRAT, J.P., ABLITZER, D., 2005. *Dust formation in electric arc furnace: Birth of the particles*. Powder Technology 157(1–3), 2–11. DOI: 10.1016/j.powtec.2005.05.006.

HAGNI, A.M., HAGNI, R.D., DEMARS, C., 1991. *Mineralogical characteristics of electric arc furnace dusts*. JOM 43(4), 28–30. DOI: 10.1007/BF03220543.

HOLLOWAY, P.C., ETSELL, T.H., 2008. *Evaluation of options for metals recovery from Altasteel EAF dust*. Canadian Metallurgical Quarterly 47(2), 149–162. DOI: 10.1179/cmq.2008.47.2.149.

KHEBRI, Z., RAZAVI, Z., SADEGHIAN, F., FAQHIHI, F., AHMADIAN, N., 2025. *A review of electric arc furnace dust (EAFD) reuse and recycle methods (waste from steel smelting and casting factories)*. Circular Economy and Sustainability 5(4), 3623–3644. DOI: 10.1007/s43615-025-00543-1.

LASTRA, R., 2002. *A comparison of liberation determinations by particle area percentage and exposed particle perimeter percentage in a flotation concentrator*. Journal of Minerals and Materials Characterization and Engineering 1(1), 31–37. DOI: 10.4236/jmmce.2002.11003.

LEIßNER, T., BACHMANN, K., GUTZMER, J., PEUKER, U.A., 2016. *A mineral liberation study of grain boundary fracture based on measurements of the surface exposure after milling*. International Journal of Mineral Processing 156, 3–13. DOI: 10.1016/j.minpro.2016.08.014.

LIN, X., PENG, Z., YAN, J., LI, Z., HWANG, J.Y., ZHANG, Y., LI, G., JIANG, T., 2017. *Pyrometallurgical recycling of electric arc furnace dust*. Journal of Cleaner Production 149, 1079–1100.

MACHADO, J.G.M.S., BREHM, F.A., MENDES MORAES, C.A., DOS SANTOS, C.A., FARIA VILELA, A.C., MARIMON DA CUNHA, J.B., 2006. *Chemical, physical, structural and morphological characterization of the electric arc furnace dust*. Journal of Hazardous Materials 136(3), 953–960. DOI: 10.1016/j.jhazmat.2006.01.044.

MARTINS, F.M., dos REIS NETO, J.M., da CUNHA, C.J., 2008. *Mineral phases of weathered and recent electric arc furnace dust*. Journal of Hazardous Materials 154(1–3), 417–425. DOI: 10.1016/j.jhazmat.2007.10.041.

MENG, Y.F., SHI, W.M., LU, C., YANG, S.Q., YANG, Q.X., DENG, J.G., 2019. *First-principles study of structural, elastic, electronic and optical properties of zinc ferrite spinel*. IOP Conference Series: Materials Science and Engineering 569, 022016. DOI: 10.1088/1757-899X/569/2/022016.

MONKHORST, H.J., PACK, J.D., 1976. *Special points for Brillouin-zone integrations*. Physical Review B 13(12), 5188–5192. DOI: 10.1103/PhysRevB.13.5188.

OUSTADAKIS, P., TSAKIRIDIS, P.E., KATSIAPI, A., AGATZINI-LEONARDOU, S., 2010. *Hydrometallurgical process for zinc recovery from electric arc furnace dust (EAFD): Part I: Characterization and leaching by diluted sulphuric acid*. Journal of Hazardous Materials 179(1–3), 1–7. DOI: 10.1016/j.jhazmat.2010.01.059.

PASQUOTO, C.G., TROVÃO, R.S., TENÓRIO, J.A.S., ESPINOSA, D.C.R., 2018. *Chemical and mineralogical characterization of electric arc furnace dust*. Proceedings of the 6th International Conference on Industrial and Hazardous Waste Management, Chania, Crete, Greece, 4–7 September 2018.

PERDEW, J.P., BURKE, K., ERNZERHOF, M., 1996. *Generalized gradient approximation made simple*. Physical Review Letters 77(18), 3865–3868. DOI: 10.1103/PhysRevLett.77.3865.

PICKLES, C.A., 2011. *Thermodynamic modeling of zinc speciation in electric arc furnace dust*. High Temperature Materials and Processes 30(1–2), 3–15. DOI: 10.1515/HTMP.2011.001.

REZENDE, A.F., de OLIVEIRA, M.C., RIBEIRO, R.A.P., MESQUITA, W.D., MARQUES, J.J., MAGALHÃES, N.F.S., LEMES, J.H.V., LONGO, E., GURGEL, M.F.C., 2022. *DFT calculations for structural, electronic, and magnetic properties of $ZnFe_2O_4$ spinel oxide: The role of exchange-correlation functional*. Materials Research 25, e20220219. DOI: 10.1590/1980-5373-MR-2022-0219.

SALCEDO RODRIGUEZ, K.L., MELO QUINTERO, J.J., MEDINA CHANDUVÍ, H.H., GIL REBAZA, A.V., FACCIO, R., ADEAGBO, W.A., HERGERT, W., RODRIGUEZ TORRES, C.E., ERRICO, L.A., 2020. *Ab-initio approach to the stability and the structural, electronic and magnetic properties of the (001) $ZnFe_2O_4$ surface terminations*. Applied Surface Science 499, 143859. DOI: 10.1016/j.apsusc.2019.143859.

SCHULZ, B. (ed.), 2021. *Applications of SEM Automated Mineralogy: From Ore Deposits over Processing to Secondary Resource Characterization*. MDPI, Basel.

SCHULZ, B., MERKER, G., GUTZMER, J., 2019. *Automated SEM mineral liberation analysis (MLA) with generically labelled EDX spectra in the mineral processing of rare earth element ores*. Minerals 9(9), 527. DOI: 10.3390/min9090527.

SOFILIC, T., RASTOVCAN-MIOC, A., CERJAN-STEFANOVIC, S., NOVOSEL-RADOVIC, V., JENKO, M., 2004. *Characterization of steel mill electric-arc furnace dust*. Journal of Hazardous Materials 109(1–3), 59–70. DOI: 10.1016/j.jhazmat.2004.02.032.

SUETENS, T., GUO, M., VAN ACKER, K., BLANPAIN, B., 2015. *Formation of the $ZnFe_2O_4$ phase in an electric arc furnace off-gas treatment system*. Journal of Hazardous Materials 287, 180–187. DOI: 10.1016/j.jhazmat.2015.01.050.

SYLVESTER, P.J., 2012. *Use of the Mineral Liberation Analyzer (MLA) for mineralogical studies of sediments and sedimentary rocks. In: Sylvester, P.J. (Ed.), Quantitative Mineralogy and Microanalysis of Sediments and Sedimentary Rocks*. Mineralogical Association of Canada Short Course Series 42, 1–16.

TRIFUNOVIC, V., MILIC, S., AVRAMOVIC, L., JONOVIC, R., GARDIC, V., DJORDJIEVSKI, S., DIMITRIJEVIC, S., 2022. *Investigation of hazardous waste: A case study of electric arc furnace dust characterization*. Hemijska Industrija 76(4), 237–249.

WANG, J., ZHANG, Y.Y., CUI, K.K., FU, T., GAO, J.J., HUSSAIN, S., ALGARNI, T.S., 2021. *Pyrometallurgical recovery of zinc and valuable metals from electric arc furnace dust: A review*. Journal of Cleaner Production 298, 126788. DOI: 10.1016/j.jclepro.2021.126788.

XUE, Y., LIU, X., XU, C., HAN, Y., 2023. *Hydrometallurgical detoxification and recycling of electric arc furnace dust*. International Journal of Minerals, Metallurgy and Materials 30(11), 2076–2094.

YAO, J.H., LI, X.H., LI, Y.W., LE, S.R., 2013. *Density functional theory investigations on the structure and electronic properties of normal spinel $ZnFe_2O_4$*. Integrated Ferroelectrics 145(1), 17–23. DOI: 10.1080/10584587.2013.788310.